


# Origin of the hysteresis of magnetoconductance in a supramolecular spin-valve based on a TbPc<sub>2</sub> single-molecule magnet

Kieran Hymas  and Alessandro Soncini \**School of Chemistry, University of Melbourne, Parkville, Victoria 3010, Australia* (Received 30 April 2020; revised 10 September 2020; accepted 14 September 2020; published 29 September 2020)

We present a time-dependent microscopic model for Coulomb blockade transport through an experimentally realized supramolecular spin-valve device driven by an oscillating magnetic field, in which the  $4f$ -electron magnetic states of an array of TbPc<sub>2</sub> single-molecule magnets (SMMs) were observed to modulate a sequential tunneling current through an underlying substrate nanoconstriction. Our model elucidates the dynamical mechanism at the origin of the observed hysteresis loops of the magnetoconductance, a signature of the SMM-modulated spin-valve effect, in terms of a phonon-assisted multi-spin-reversal cascade relaxation process, which mediates the switching of the device between the two conductive all-parallel spin configurations of the SMM array. Moreover, our proposed model can explain the zero-bias giant magnetoresistive transport gap measured in this device, solely within the incoherent transport regime, consistently with the experimental observations, as opposed to previous interpretations invoking Fano-resonance conductance suppression within a coherent ballistic transport regime. Finally, according to the proposed Coulomb blockade scenario, the SMM-mediated giant magnetoresistance effect is predicted to increase with the number of SMMs aligned on the nanoconstriction surface, on account of the increased number of intermediate nonconducting spin-flip states intervening in the phonon-assisted multi-spin-reversal cascade relaxation process necessary to switch between the two conducting all-parallel SMM spin configurations.

DOI: [10.1103/PhysRevB.102.125310](https://doi.org/10.1103/PhysRevB.102.125310)

## I. INTRODUCTION

In the wake of Fert and Grünberg's late-1980s discovery of the giant magnetoresistance effect [1,2], thin-film spin-valves have undergone a rapid transition from the laboratory to their incorporation into commercial devices such as magnetic random-access memory devices and read-heads for high density hard drives. To further the pursuit for the ultimate miniaturization of electronic devices, molecular analogs of the spin-valve have been studied where one or both of the bulk ferromagnetic domains of the device are replaced by a single (or few) magnetic molecules [3–7].

Molecular spin-valve devices based on the lanthanide single-molecule magnet (SMM) bis-(phthalocyaninato) terbium(III) (TbPc<sub>2</sub>) [8–10] have been experimentally realized in graphene nanoconstriction [11] and carbon nanotube (CNT) [12–14] spintronics setups wherein highly anisotropic hysteresis loops of magnetoconductance emerge when a magnetic field aligned along the easy axis of the molecules is traced and retraced over the device. Given the anisotropic nature of the magnetoconductance signals observed in the terbium spin-valve experiments as well as in other TbPc<sub>2</sub> molecular devices [15,16], the existence of an exchange interaction between the terbium ion and conduction electrons delocalized across the phthalocyanine ligands of the molecule has been proposed.

The sign and magnitude of this exchange interaction has been probed in spintronics set-ups [17], in high-field EPR experiments [18], and corroborated by multiconfigurational

[19] and multireference [20] *ab initio* calculations, all revealing a ferromagnetic coupling between Tb(III) and a spin- $\frac{1}{2}$  radical delocalized across the phthalocyanine ligands of the order of  $0.1 \text{ cm}^{-1}$ . The presence of a radical spin delocalized over the Pc<sub>2</sub> organic ligands in the neutral oxidation state [TbPc<sub>2</sub>]<sup>0</sup> of this SMM, and its ferromagnetic exchange coupling to the  $4f$  electrons of the Tb(III) ion, has been argued to mediate spin interactions between the localized Ln(III) magnetic moment and underlying substrates, such as magnetic thin films [21–23] or the conduction electrons carrying the electric current in the carbon nanostructures underpinning some molecular spintronics devices [11–16,24]. Notably, this exchange coupling has been argued to be at the origin of a weakly decohering readout of a single TbPc<sub>2</sub> nuclear qubit [25].

In the spin-valve setup of interest in this paper, the ferromagnetic exchange coupling has been implicated in a microscopic spin-transport mechanism that gives rise to a strongly anisotropic giant magnetoresistance effect, accounting for sharp jumps of the conductance of the carbon nanoconstriction as a function of a time-dependent sweeping longitudinal magnetic field, which orients the magnetic moments of the grafted TbPc<sub>2</sub> molecules parallel to the field and to each other [11,13,26]. Crucially, the observed effect is intrinsically kinetic, also displaying a memory dependence in that, for a given sign of the magnetic field, two sharp jumps of the magnetoconductance are only observed upon tracing the field (i.e., while the field grows from zero to its maximal value along a given direction) and not upon retracing (when the field is decreased from its maximal value back to zero). A symmetric situation is then observed upon dynamical reversal of the

\*asoncini@unimelb.edu.au

field direction. This gives rise to the typical hysteresis loop of the magnetoconductance which, together with its strongly anisotropic character, is the hallmark of the SMM signature on the transport properties of the carbon nanoconstriction.

Early interpretations reported in the original experimental works [11–13] pointed at the need to have at least two SMMs grafted on the carbon nanoconstriction device to observe the spin-valve effect. The reasoning was based on similar arguments explaining the workings of thin-film spin-valves, thus on the expectation that the antiparallel orientation of the molecular magnetic moments expected in low magnetic fields, where the two conductance jumps are observed, leads to reduced transmission of charge carriers with either spin projection, resulting in a blocking of the conductance and the onset of giant magnetoresistance. Conversely, a strong magnetic field will orient the molecular spins parallel to the field (and hence to each other), thus quenching the destructive interference between opposite spin carriers and greatly enhancing the differential conductance of the device.

These early intuitions were at first rationalized by Hong and Kim in 2013 using broken-symmetry Density functional theory (DFT) calculations to simulate ballistic transport linear response of a model (6,6)-nanotube device, consisting of 24 unit cells in the scattering region, with two vanadocene complexes with spin polarization forced to be either parallel or antiparallel to each other [27]. The authors found that while oppositely spin-polarized molecules would induce transmission dips and corresponding halving of conductance for scattering electrons of both spin polarizations provided they have an energy matching the molecule-projected density of states resonances, two vanadocene molecules with parallel spin polarization (simulating high magnetic field conductance) could only reduce the transmission of like-spin conduction electrons and leave unaffected the transmission of electrons with opposite spin polarization. The effect was interpreted as a spin-dependent Fano-resonance suppression of conductance.

Questions remain as to whether a purely coherent transport model, which is a necessary condition to invoke a destructive interference effect such as spin-dependent Fano resonance, and which implies a strong coupling between leads and device, can be fully consistent with the experimental observation of a Coulomb blockade transport regime in molecular spin-valve setups [11–13] that epitomizes a quintessential noncoherent sequential tunneling transport regime.

The question of integrating noncoherent transport into the proposed Fano-resonance model was later addressed in a 2017 work by Krainov *et al.* [26], where additional experimental features such as the opening up of a transport gap in the Coulomb blockade stability diagram in zero field were highlighted and rationalized by further elaborating on the spin-dependent Fano-resonance model proposed in 2013 [27]. In particular, a spin-dependent Fano resonance with a state localized within a ballistic one-dimensional double barrier scattering problem was invoked both as a transport mechanism explaining the transport gap in zero field and also as the mechanism responsible for the partitioning of the CNT device into sequences of spin-dependent quantum dot islands. Such quantum dot islands were then mapped into a system of classical capacitors in a phenomenological model, establishing the

energetics of sequential charging and discharging processes, then utilized to set up a somewhat featureless spin-dependent sequential tunneling transport model in the presence or absence of a magnetic field.

While previous theoretical models [26–28] captured specific features of the reported supramolecular spin-valve transport experiments [11,13], these models did not integrate a comprehensive description of all available experimental information. In particular, previous works did not address some key aspects related to the TbPc<sub>2</sub> SMM electronic structure and ensuing dissipative spin dynamics, which are arguably significant in this particular transport experiment, performed at cryogenic temperatures and in the presence of a time-dependent oscillating magnetic field. (i) The first aspect is the role played by the 4*f*-Pc<sub>2</sub> radical exchange energy scale in the microscopic transport mechanism. (ii) The second aspect consists of the time-dependent nature of the dissipative SMM spin dynamics affected by spin-phonon coupling, which results in the observed hysteresis of the magnetoconductance. (iii) The third and final aspect consists of the dependence of the spin-valve transport dynamics on the number of aligned molecular nanomagnets in the SMM array and the discussion of the underlying microscopic mechanism.

In the attempt to formulate a full comprehensive picture of quantum transport in this molecular spin-valve device that is consistent with all experimental observations reported thus far, we propose here a time-dependent dissipative microscopic model based on quantum master equations, which fully accounts for the observed noncoherent Coulomb blockade transport regime and for the observed hysteresis of the magnetoconductance signature of a kinetic molecular spin-valve effect. The proposed model explicitly includes all those ingredients that were disregarded in previous theoretical works, namely, (i) the energy scale of the Tb(III) 4*f*-Pc<sub>2</sub> radical/conduction electron ferromagnetic exchange coupling, explicitly included in the microscopic Hamiltonian of the device quantum states, (ii) the effect on the noncoherent transport processes of the interplay between the time-dependent driving force of the oscillating longitudinal magnetic field and the dissipative SMM spin-phonon relaxation dynamics, and (iii) the study of the transport dynamics as function of the size of the SMM array.

As in the model proposed by Krainov *et al.* [26], in our model we also assume the device is partitioned into a series of quantum dots, each dot defined by the presence of one TbPc<sub>2</sub> SMM. However, here we assume that the source of incoherent hopping in the transport process originates solely at the lead-device interface (thus assuming weak lead-device coupling), while the sequence of quantum dots in which the whole supramolecular nanojunction structure is partitioned by the interaction with the grafted TbPc<sub>2</sub> nanomagnets is assumed to be described in terms of coherent multielectronic states, whose occupation fluctuates during the sequential tunneling transport process. In other words, the sequential array of hybridized TbPc<sub>2</sub>-dot states in our model is not represented in terms of a number of incoherently coupled quantum dot islands [26] but rather they are described as a chain formed by an arbitrary number of localized orbital basis functions, generalizing recently proposed electronic structure setups limited to two molecules only [28] to an arbitrary number of localized

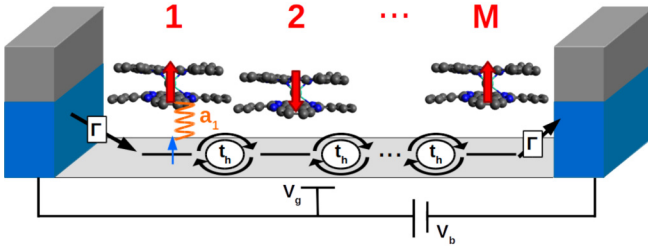


FIG. 1. A schematic for the supramolecular spin-valve device, where  $M$  TbPc<sub>2</sub> nanomagnets are adsorbed on a chain of  $M$ -coupled quantum dots forming the nanoconstriction junction. Conduction electrons tunnel onto the device incoherently from nearby electrodes at a rate  $\Gamma$  and hop coherently along the chain of dot nanomagnets with amplitude  $t_h$ , experiencing a local Ising exchange interaction  $a_i$  with the  $4f$  quantum states of each Tb(III) center.

electronic states, which can be linearly combined into states delocalized over the full extent of the nanoconstriction.

We show that our dissipative dynamical model is capable of reproducing the observed hysteresis of the magnetoconductance, offering an explanation of the kinetic molecular spin-valve effect as manifested through the observed jumps of the magnetoconductance, one that is based on the interplay between multiple Tb(III) spin-relaxation processes in the driving sweeping field. Furthermore, we will also show that our model is able to reproduce the transport gap observed in zero magnetic field without invoking ballistic Fano-resonance transport events and to provide some predictions as to the scaling of the magnetoresistance effect with the number of molecules in the spin-valve device.

## II. THEORETICAL MODEL OF THE SPIN-VALVE

### A. Spin-valve Hamiltonian

The device is comprised of a chain of  $M$  TbPc<sub>2</sub> molecules adsorbed to an sp<sup>2</sup> hybridized surface (modeled here as several quantum dots in series) and subject to an oscillating magnetic field  $\mathbf{B}(t)$  as well as a static electric potential  $V_g$  from a nonlocal gate electrode. A bias voltage  $V_b$  is applied to two leads (electrodes) that sandwich the scattering region, facilitating electron transport through the device. A schematic of the device for  $M$  molecules grafted to the nanoconstriction is shown above in Fig. 1.

In particular, we approximate the relevant electronic states of the nanojunction with  $M$  TbPc<sub>2</sub> molecules sequentially grafted onto its surface in terms of a set of  $M$  states sequentially localized between the two leads, each subband hybridized with one singly occupied molecular orbital state of the Pc ligand of the TbPc<sub>2</sub> molecule grafted on that section of the substrate. These one-electron dot-molecule states are assumed to be orbitally nondegenerate, hence they can be empty ( $N$  electron charge state), occupied by one electron of either spin ( $N + 1$  electron charge state), or occupied at most by two spin-paired electrons ( $N + 2$  electron charge state). The spin moment of the electrons occupying the dot-molecule hybridized states, in turn, are exchange coupled to the local Tb(III)  $4f$  electrons, described by the doubly degenerate ground Ising doublet  $|J = 6, m_J = \pm 6\rangle$ , which is

well known to be thermally well isolated from other excited crystal field states belonging to the same strongly split <sup>7</sup>F<sub>6</sub> spin-orbit multiplet [8,9,19,20,29]. The energy scale of the exchange coupling between the spin of the fluctuating charge on the dot-Pc subband and the Tb(III)  $4f$  electrons for the  $i$ th site is described by the coupling constant  $a_i$  and assumed to be ferromagnetic as in the case of the isolated [TbPc<sub>2</sub>]<sup>0</sup> molecule [18–20], thus favoring parallel orientation between the spin on the Pc ligand (here delocalized over the local dot-Pc state) and the  $4f$ -electron magnetic moment.

With this assumption, the low-energy spectrum of a chain of  $M$  TbPc<sub>2</sub> molecules adsorbed onto the series of underlying quantum dots and subject to an oscillating magnetic field is captured with the Hamiltonian

$$H_s(t) = \sum_{i=1}^M [(\epsilon_i - eV_g)c_{i\sigma}^\dagger c_{i\sigma} + U n_{i\uparrow} n_{i\downarrow} - a_i J_z^i s_z^i] + \sum_{(ij)} t_h^* c_{i\sigma}^\dagger c_{j\sigma} + \text{H.c.}, \quad (1)$$

where the first sum runs over all  $M$  dot-molecule sites and the second sum runs over nearest-neighbor dot-molecule sites, i.e., it describes coherent hopping with amplitude  $t_h$  along the chain of dot-molecule site orbitals. The first term represents the single electron occupancy energy of each quantum dot modified by the gate voltage  $V_g$ . Here,  $c_{i\sigma}^{(\dagger)}$  annihilates (creates) an electron with spin  $\sigma$  on the  $i$ th quantum dot. The second term is weighted by an on-site Coulomb integral  $U$  accounting for electronic repulsion between two spin-paired electrons at a given site;  $n_{i\sigma} = c_{i\sigma}^\dagger c_{i\sigma}$  are the number operators for spin  $\sigma$  at site  $i$ . The third term describes the exchange interaction between the Tb(III) nanomagnet at site  $i$  and the spin of the  $i$ th quantum dot.  $J_z^i$  and  $s_z^i$  are the total and spin-only angular momentum projection operators along the TbPc<sub>2</sub> magnetic anisotropy axis for the Tb(III)  $4f$  electrons and the Pc-dot electron, respectively (a Heisenberg exchange Hamiltonian would be projected into this simpler Ising coupling Hamiltonian due to the highly axial nature of the Tb(III) ground state), while  $a_i$  denotes the magnitude and sign of the  $4f$ -Pc radical exchange coupling at the  $i$ th site. Notably, we have assumed here for simplicity that all of the nanomagnets in the chain share the same quantization axis (the device  $z$  axis). This is a reasonable assumption, owing to the favorable interaction between the sp<sup>2</sup> hybridized substrate and the bulky pyrene anchors that are covalently attached to the Pc ligands of each nanomagnet [30]. Nonetheless, in Appendix A we relax this constraint and show that the inclusion of disordered nanomagnet quantization axes can lead to a quenching of the kinetic spin valve for large tilting angles. The penultimate term is the Zeeman interaction between the total magnetic moment of the device and the longitudinal component of an external oscillating magnetic field  $B_z(t)$ .

To explicitly account for the interplay between the spin dynamics driven by the oscillating magnetic field, the sequential tunneling dynamics, and the slow magnetic relaxation of the TbPc<sub>2</sub> nanomagnets, we also introduce a model Hamiltonian accounting for the coupling between the nanomagnet spin and the acoustic phonons of the underlying 2D substrate. Thus the quantized lattice vibrations of the substrate couple weakly to

the angular momentum states of TbPc<sub>2</sub> via small perturbations to each molecule's ligand field [31], as embodied to first order in the spin-phonon coupling Hamiltonian [32]

$$H_{\text{sp}} = \sum_{i=1}^M \sum_{\mathbf{q}} \frac{\partial H_{\text{cf}}^i}{\partial Q_{\mathbf{q}}^i} \Big|_0 Q_{\mathbf{q}}^i, \quad (2)$$

where  $Q_{\mathbf{q}}^i$  corresponds to the contribution of the active molecular normal mode of vibration for the  $i$ th molecule to the device phonon eigenmode of wave vector  $\mathbf{q}$  and  $H_{\text{cf}}^i$  is the equilibrium crystal field Hamiltonian for the  $i$ th nanomagnet. The device is also coupled to two electrodes modeled here as semi-infinite, noninteracting electron reservoirs with  $H_l = \sum_{\alpha k \sigma} \varepsilon_{\alpha k \sigma} a_{\alpha k \sigma}^\dagger a_{\alpha k \sigma}$ , where  $a_{\alpha k \sigma}^{(\dagger)}$  destroys (creates) an electron in lead  $\alpha$  with wave vector  $\mathbf{k}$ , spin  $\sigma$ , and energy  $\varepsilon_{\alpha k \sigma}$ . We describe tunneling of electrons into and out of the scattering region with the Hamiltonian [33]

$$H_T = \sum_{i=1}^M \sum_{\alpha k \sigma} T_{\alpha,i}^* a_{\alpha k \sigma}^\dagger c_{i\sigma} + \text{H.c.} \quad (3)$$

In principle, electrons may tunnel from an electrode to any site  $i$  on the substrate (and vice versa) with amplitude  $T_{\alpha,i}$ , however, we restrict our model to the most likely case for the given experimental setup, namely, where  $T_{\alpha,i} = 0 \forall i \neq 1, M$ .

In this paper, we investigate the Coulomb blockade transport regime for a device described by the Hamiltonians Eqs. (1)–(3), exploring in particular two  $N/N+1$  and  $N+1/N+2$  charge resonances, giving rise to a sequential tunneling current. Furthermore, we shall investigate the effect on our model of increasing the chain length  $M$ . To understand the simplest regime, we place great emphasis on the  $N/N+1$  resonance obtained by assuming that only  $M=2$  nanomagnets are grafted on the nanojunction, which will allow us later to draw generalized conclusions for a larger number of nanomagnets. In the case  $M=2$ , Eq. (1) can be diagonalized exactly, and we are able to obtain the most pertinent physics of the molecular spin valve. When both dots in the scattering region are vacant, the instantaneous eigenstates of  $H_s(t)$  are uncorrelated products of the terbium spin states  $|m_{J,1}, m_{J,2}\rangle$  where each  $m_{J,i} = \pm J$  with time-dependent Zeeman energy  $E_0(m_{J,1}, m_{J,2})$  for a nonzero oscillating magnetic field in the adiabatic approximation. When the device is charged by a conduction electron with spin  $\sigma$ , due to the Ising character of the exchange coupling and the assumption that the external field is aligned along the magnetic anisotropy axes of the nanomagnets, all spin and total angular momenta quantum numbers  $\sigma$ ,  $m_{J,1}$ , and  $m_{J,2}$  remain good quantum numbers (i.e., the Hamiltonian in Eq. (1) commutes with  $J_1$ ,  $J_2$  and  $\sigma$  angular momentum and spin operators) so the instantaneous eigenstates of  $H_s(t)$  become  $|m_{J,1}, m_{J,2}, \sigma, \pm\rangle = |m_{J,1}, m_{J,2}\rangle \times [u^\pm(m_{J,1}, m_{J,2}, \sigma) |\sigma\rangle_1 |0\rangle_2 + v^\pm(m_{J,1}, m_{J,2}, \sigma) |0\rangle_1 |\sigma\rangle_2]$ , where  $|\sigma\rangle_i$  denotes the occupancy of site  $i$  with an electron of spin  $\sigma$ ; the energy of these states are denoted  $E_1(m_{J,1}, m_{J,2}, \sigma, \pm)$  and can be found in Appendix B. Consequently, a conduction electron that charges the scattering region (regardless of spin) becomes delocalized across both sites 1 and 2 interacting with both Tb moments via the exchange coupling  $a_i$ . If we consider  $a_1 = a_2 = a > 0$ ,

then the fully polarized (parallel) configurations of the Tb moments  $|J, J, \uparrow, -\rangle$  and  $|-J, -J, \downarrow, -\rangle$  become the degenerate ground states of the singly charged manifold at zero applied longitudinal field. The exact, generalized expressions for the energies and amplitudes of these redox states are given in Appendix B.

## B. Time-dependent transport in the adiabatic approximation

To model the transport dynamics of the spin valve in the presence of a time-dependent longitudinal magnetic field, we develop adiabatic rate equations [34] to first (nonvanishing) order in the spin-phonon Hamiltonian from Eq. (2), and the transport Hamiltonian from Eq. (3), for the diagonal elements of the reduced density matrix  $\rho$  expressed on the basis of the eigenstates of  $H_s(t)$ . The rate equation for the population of an  $H_s(t)$  eigenstate  $|q\rangle$  reads

$$\dot{\rho}_q = \sum_r (W^{r \rightarrow q} + \Omega^{r \rightarrow q}) \rho_r - \sum_r (W^{q \rightarrow r} + \Omega^{q \rightarrow r}) \rho_q. \quad (4)$$

The time evolution of the diagonal elements of the reduced density matrix in Eq. (4) is governed by two processes: (i) the rates of charging and discharging of electrons from the leads onto the device  $W^{r \rightarrow q}$  and (ii) the phonon-mediated Tb magnetic moment flipping rates  $\Omega^{r \rightarrow q}$ , which are both time-dependent quantities owing to the oscillating field. More explicitly, the charging transition rate between a state  $|q\rangle$  and a state  $|r\rangle$  (differing by one electron on the device) induced by  $H_T$  is given by

$$W^{q \rightarrow r} = \sum_{\alpha i \sigma} \frac{\Gamma_{\alpha,i}}{2} |c_{i\sigma,rq}^\dagger|^2 \int_{-\infty}^{\infty} \frac{d\varepsilon}{\sqrt{2\pi\xi}} e^{-\left(\frac{\varepsilon - \omega_{rq}}{\xi}\right)^2} f(\varepsilon - \mu_\alpha), \quad (5)$$

with the rates summed over the two leads  $\alpha = L, R$ , sites  $i$ , and conduction electron spin  $\sigma$ . Here,  $\Gamma_{\alpha,i} = 2\pi D_\alpha |T_{\alpha,i}|^2$  is the coupling strength between the  $i$ th dot and lead  $\alpha$  with the constant density of states  $D_\alpha$  and  $c_{i\sigma,rq}^\dagger = \langle r | c_{i\sigma}^\dagger | q \rangle$  is the transition amplitude. The transition rates depend on the number of available electrons with energy  $\varepsilon$  in lead  $\alpha$  which is given by the Fermi-Dirac distribution  $f(\varepsilon - \mu_\alpha) = [1 + \exp((\varepsilon - \mu_\alpha)/k_B T)]^{-1}$  evaluated at the bias voltage  $\mu_\alpha = \pm V_b/2$ ; the upper (lower) sign refers to the source (drain) electrode. The electronic levels of the molecular system are broadened by a Gaussian line shape centered at the time-dependent energy gap  $\omega_{rq}$  to account for the finite linewidth acquired by coupling the system to the continuum of states in the leads [35]. The discharging rate from  $|r\rangle$  to  $|q\rangle$  is obtained from Eq. (5) with the substitutions  $c_{i\sigma,rq}^\dagger \mapsto c_{i\sigma,qr}$  and  $f(\varepsilon - \mu_\alpha) \mapsto [1 - f(\varepsilon - \mu_\alpha)]$ . Incoherent transitions induced by the absorption or emission of lattice phonons are described with a two-dimensional Debye model and are calculated using the formula

$$\Omega^{q \rightarrow q'} = \pm \gamma_{\text{sp}} \frac{\omega_{q'q}^2}{1 - \exp(\omega_{q'q}/k_B T)}, \quad (6)$$

where the  $\pm$  takes into account phonon absorption or emission and  $\gamma_{\text{sp}}$  is the spin-phonon coupling constant. The microscopic nature of this direct transition is discussed in Appendix C.



We assume here that only single phonons can be absorbed (emitted) from (to) the lattice such that only a single Tb moment may be flipped at a time [34] so, for example,  $\Omega_{|J,J\rangle \rightarrow |-J,-J\rangle} = 0$  whereas  $\Omega_{|J,J\rangle \rightarrow |J,-J\rangle} \neq 0$ . The matrix elements for each transition are absorbed into the coupling constant  $\gamma_{\text{sp}}$  and are not evaluated explicitly. Finally, note that the phonon transition rates, like the charging/discharging rates, depend on the gaps  $\omega_{qq'}$ , hence they are also time-dependent quantities.

In Eq. (4), we have neglected the contribution of nonsecular terms (that is, terms that couple the populations and coherences of the density matrix) to the evolution of  $\rho_q$  on the grounds that away from degeneracies these contributions oscillate for several cycles on the timescale of the course-grained evolution assumed for the Markovian master equation in Eq. (4) and thus integrate to zero. At degeneracy, however, where nonsecular terms cannot in general be ignored, we discard these contributions to the spin dynamics on alternative grounds. The nonsecular terms originating from the spin-phonon coupling in Eq. (2) are weighted by thermal factors that, at the low temperatures explored in molecular spintronics experiments, greatly suppress their contributions around the degeneracy. For the  $N$  electron manifold, nonsecular terms arising from the hybridization to the leads due to Eq. (3) are proportional to  $\sum_{\sigma} \langle r | c_{\sigma} | v \rangle \langle v | c_{\sigma}^{\dagger} | q \rangle$ , where  $|r\rangle$  is a state from the same charge manifold as  $|q\rangle$ . Since charging and discharging an electron via the reduced state  $|v\rangle$  cannot modify the configuration of the terbium moments these terms are only nonzero when the  $H_s(t)$  eigenstates  $|r\rangle$  and  $|q\rangle$  are one in the same; such a scenario corresponds to a secular term which is defacto included in Eq. (4). A similar argument can be made for nonsecular corrections to the dynamics of states in the  $N + 1$  manifold.

Due to the complexity of the ensuing adiabatic rate equation, we resort to numerical integration of Eq. (4) to find the time evolution of the diagonal elements  $\rho_q$ . For sufficiently long times, the solutions to Eq. (4) tend to a limit cycle, recurring with the period of the oscillating field; in other words, they display a hysteresis dynamics which is independent of the initial conditions. With the solutions to the adiabatic rate equations in tow, the time-dependent magnetoconductance  $g$  of the molecular spin valve is evaluated by taking the derivative with respect to bias voltage of the time-dependent current given by [36,37]

$$I_L = e \sum_{qr} (N_r - N_q) \rho_q W_L^{q \rightarrow r}, \quad (7)$$

where  $N_q$  and  $N_r$  are the number of electrons on the device for the states  $|q\rangle$  and  $|r\rangle$ , respectively, and  $W_L^{q \rightarrow r}$  are charging/discharging rates from/to the left electrode only.

### III. RESULTS AND DISCUSSION

#### A. Hysteresis of the magneto-conductance and dynamical spin-valve effect

For the purposes of our calculations, we choose  $a = 0.02$  meV as obtained from transport experiments on a terbium molecular spin transistor [17], we set  $\epsilon_1 = \epsilon_2 = \epsilon$ ,  $t_h = 5$  meV,  $\xi = 0.05$  meV and explore the operation of the de-

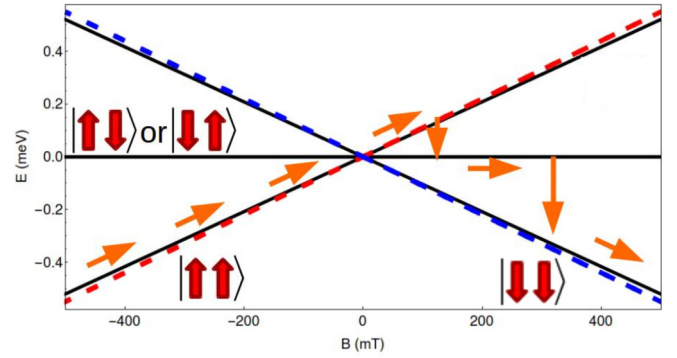


FIG. 2. Zeeman energies of the lowest lying energy levels of the TbPc<sub>2</sub> molecular spin valve. The solid black lines represent uncharged states of the device with the magnetic moments of each TbPc<sub>2</sub> nanomagnet labeled with thick, red arrows. The blue (red) dashed lines represent the corresponding ferromagnetic states for the parallel  $| -J, -J, \downarrow \rangle$  ( $| J, J, \uparrow \rangle$ ) states. Orange mechanistic arrows are included to illustrate population transfer between the states when a magnetic field is traced from negative to positive values across the device, thus leading to the two sharp jumps in magnetoconductance, characteristic of the molecular spin-valve experiments.

vice in the presence of a sinusoidally oscillating magnetic field  $B_z(t) = B_z \sin(\omega t)$  aligned along the easy axes of  $M = 2$  Tb nanomagnets with amplitude  $B_z = 500$  mT. With this choice of parameters, the most relevant states for low temperature and low bias electron transport through the spin valve have been plotted in Fig. 2. The coupling strength between the carbon nanoconstriction region and the leads can be expressed in matrix form as

$$\Gamma = \begin{pmatrix} \Gamma_{S,1} & \Gamma_{S,2} \\ \Gamma_{D,1} & \Gamma_{D,2} \end{pmatrix} = \Gamma \begin{pmatrix} 1 & 0 \\ 0 & 1 \end{pmatrix}, \quad (8)$$

assumed here to be weighted by a lead-junction tunneling rate  $\Gamma = 10^4$  s<sup>-1</sup>. We note that our calculations remain largely invariant, if only for a renormalization of the magnetoconductance magnitude, to the choice of  $\Gamma$  provided that single-electron charging and discharging rates are much faster than the sweeping rate of the magnetic field (i.e.,  $\Gamma \gg \omega$ ). Calculations were performed with a spin-phonon coupling  $\gamma_{\text{sp}} = 1$  meV<sup>-2</sup> s<sup>-1</sup> and at  $T = 0.5$  K. As will become apparent in the following discussion, the particular value of the spin-phonon coupling  $\gamma_{\text{sp}}$  is not crucial for the observation of hysteresis loops of the magnetoconductance in our calculations, but rather it is the ratio between  $\gamma_{\text{sp}}$  and the magnetic-field sweeping rate  $\omega$  that gives rise to the loops of conductance.

To begin our discussion of the molecular spin valve, we specialize to the  $N/N + 1$  resonance and choose  $V_g$  so as to bring the  $N + 1$  electron ferromagnetic ground states for the reduced system to level degeneracy with the ground states of the neutral system at zero field. In Fig. 3, we report the calculated magnetoconductance as a function of the oscillating magnetic field, highlighting the tracing (blue) and the retracing (red) sweep phases, for several field sweep rates. When the magnetic field is traced across the device, the conductance remains constant until an abrupt decrease and

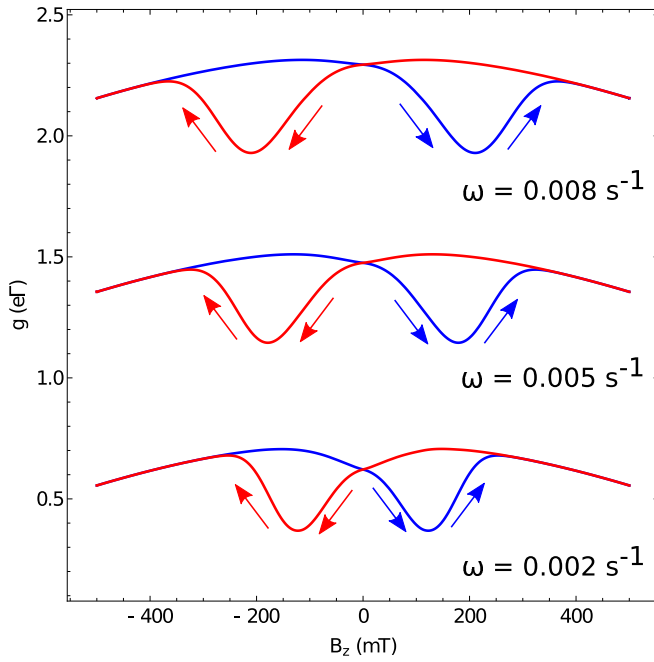


FIG. 3. Conductance loops of hysteresis on field tracing (blue) and retracing (red) obtained at different field sweep rates  $\omega$ . The top (bottom) curves have been shifted by  $+(-)0.8e\Gamma$  for clarity.

subsequent recovery is observed after crossing zero field. The same behavior is observed on retracing the longitudinal field, hence giving rise to loops of hysteresis in the conductance. We thus immediately note that our model is capable of capturing the spin-valve-like dynamic hysteretic behavior observed in experiments [11,13]. As the rate of the sweeping field and their minima occur at larger magnitudes of the applied field. When the rate of the sweeping field is decreased, the converse is true and, in fact, the conductance begins to fall before zero field.

To understand the origin of the loops of hysteresis in the calculated conductance shown in Fig. 3, consider a field tracing event in the long-time limit. At the beginning of the trace, we have  $B_z \sin(\omega t) < 0$ , so the ground-state configuration of the spin valve consists of parallel Tb moments aligned against the field:  $|J, J\rangle$ . As can be observed from Fig. 2, since  $E_1(J, J, \uparrow, -) \approx E_0(J, J)$ , the level degeneracy condition is satisfied and a finite conductance is observed through the device. As the field is traced through  $B_z \sin(\omega t) = 0$ ,  $|J, J\rangle$  becomes an excited state of the system and phonon-mediated relaxation to  $|J, -J\rangle$  and  $|-J, J\rangle$  begins to play a role. Owing to the ferromagnetic exchange coupling  $a$ , the charged state  $|\pm J, \mp J, \sigma, -\rangle$  is thermally inaccessible for transport leading to a suppression of the conductance. At positive fields,  $|\pm J, \mp J\rangle$  is still an excited state of the device, and a phonon-induced relaxation to the  $|-J, -J\rangle$  ground state is observed, but only for positive magnetic field values of  $\sim 100$  mT since, as per Eq. (6), the phonon emission relaxation process grows quadratically with the energy of the released phonon. As in the time-reversed configuration, the  $|-J, -J, \downarrow, -\rangle$  satisfies the level degeneracy condition with  $|-J, -J\rangle$  and the

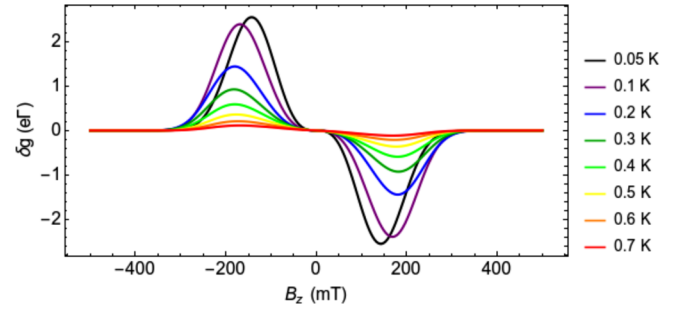


FIG. 4.  $\delta g$  for a given field tracing and retracing event calculated at various temperatures with a sweeping rate of  $\omega = 0.005$  s $^{-1}$ .

conductance is resumed to its normal value before completion of the trace.

Note that this configures a two-step magnetoconductance drop and then revival, where the drop occurs in the proximity of zero magnetic field as observed in experiment (depending also on the field sweep rate), while the revival of the current occurs for  $B_z \sim 200$  mT, which compares well with the value observed for the nanomagnet-based spin-valve experiments on a graphene nanoconstriction [11]. This procedure replays on retracing the field, however, now with the Tb configurations reversed and the drop in conductance appearing toward the other side of zero field. The timescales of the sweeping field and the phonon-mediated slow relaxation of the spin valve through the intermediate nonconducting  $|\pm J, \mp J\rangle$  states are hence inextricably linked, as expected for a hysteresis of the sequential tunneling conductance driven by the slow magnetic relaxation of the TbPc $_2$  magnetization. The faster the sweeping field, the further apart the conductance-suppressing and the conductance-reviving phonon transitions appear, leading to broader loops of hysteresis as shown in Fig. 3.

To further the investigation of the hysteresis loops of conductance, it becomes useful to define a quantity  $\delta g = g_{\text{trace}} - g_{\text{retrace}}$  that characterizes the sign of the loops for some trace-retrace cycle in the long-time limit. In Fig. 4, we show that the opening of the hysteresis loops of conductance is temperature sensitive, with the loops closing completely around  $T = 0.7$  K as observed in experiments [13]. The spin-valve effect is quenched when  $k_B T \sim a$  as the  $|\pm J, \mp J, \sigma, -\rangle$  states become thermally accessible for charge transport, hence the antiparallel Tb configurations become electrically conductive. As all configurations of the nanomagnet moments are electrically conductive above this temperature, the magnetoconductance becomes insensitive to phonon-mediated population transfer between different spin-flip configurations of the nanomagnet array, so the kinetic spin-valve effect is lost. Thus the energy scale of the exchange coupling between  $4f$  electrons and the sequential tunneling electrons fixes the temperature range for the observation of the supramolecular spin-valve effect. We also investigated the effect on  $\delta g$  of detuning the gate voltage  $V_g$  by  $\delta V_g$  away from the  $E_0(J, J) = E_1(J, J, \uparrow, -)$ -level degeneracy, and found that the sign of  $\delta g$  is preserved when crossing the level degeneracy, as shown in Fig. 5, in agreement with experimental findings [11,13].

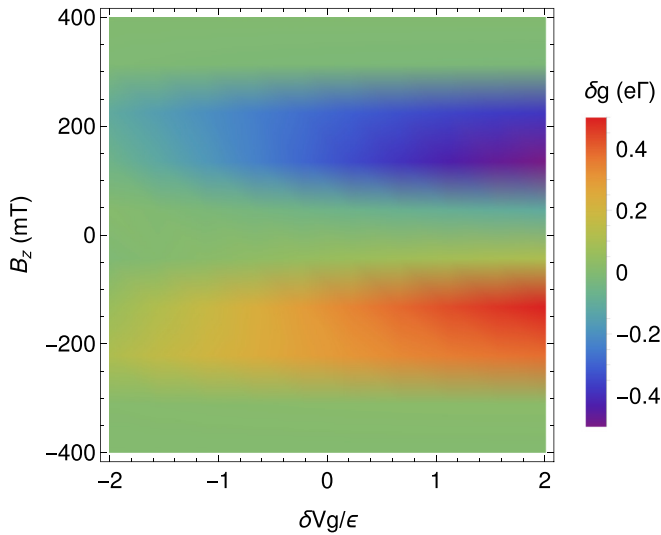


FIG. 5.  $\delta g$  as a function of the dynamically sweeping field amplitude  $B_z$  and gate voltage detuning  $\delta V_g$  away from the  $E_0(J, J) = E_1(J, J, \uparrow, -)$  level degeneracy.

### B. Generalized dynamical model: Multiple nanomagnets, steady-state conductance, and higher charge states

In addition to the simplest case when  $M = 2$ , we also investigated the effect of increasing the SMM array length  $M$ . Figure 6(b) reports the hysteresis of the differential conductance we calculated for the spin-valve device encompassing arrays of  $M$  TbPc<sub>2</sub> dot-molecule units, with  $M = 2$ ,  $M = 3$ , and  $M = 4$ . We note that while the field value at which the conductance reaches its minimum upon tracing and retracing remains invariant with increased chain length  $M$ , the percentage drop in conductance increases as more dot-molecule units are included in the model. Thus our model predicts that the giant magnetoresistance effect will increase with the number of nanomagnets aligned along the spin-valve device, as predicted in a previous theoretical treatment of the nanomagnet device, which, however, was based on the ballistic transport regime [27]. Furthermore, for  $M > 2$  we observe a gradual fall in the conductance before zero field upon tracing and retracing, following the usual precipitous drops in conductance already described above.

The microscopic mechanism leading to the increased dynamical magnetoresistance effect with increased  $M$  can be readily rationalized as follows. Including  $M$  sequential TbPc<sub>2</sub> nanomagnets into the molecular spin valve has the effect of introducing  $2^M - 2$  nonconducting configurations of the Tb moments that must be parsed via phonon-mediated population transfer when switching between the conducting all-parallel configurations  $|J, \dots, J\rangle$  and  $|-J, \dots, -J\rangle$ , with the sweeping magnetic field [see Fig. 6(a)]. The larger drop in conductance during the phonon-mediated slow relaxation of the spin valve with increased  $M$  can then be attributed to greater population transfer out of the conducting parallel configuration and into the set of  $2^M - 2$  spin-flip nonconducting microstates of the device in a multistep spin-lattice relaxation cascade. A similar argument accounts for the pre-zero-field decline in conductance whereby phonon absorption occurs to a small degree

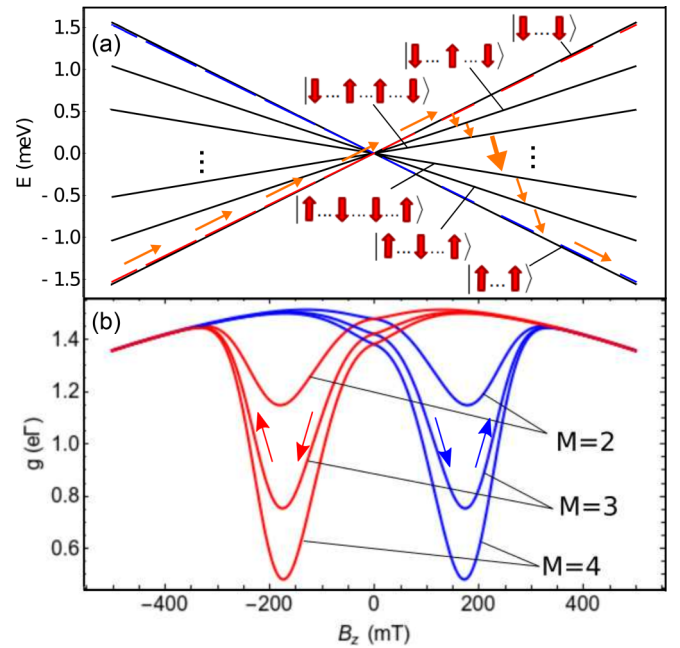


FIG. 6. (a) Magnetic-field dependence of the lowest lying energy levels of the TbPc<sub>2</sub> spin-valve device with  $M$  nanomagnets in series. As in Fig. 2, the solid black lines represent uncharged states of the device and are labeled by the spin polarization of the TbPc<sub>2</sub> units (red arrows, some configurations have been omitted to ease visualization). The dashed lines (blue and red) represent the corresponding ferromagnetic reduced states for the parallel configurations  $|\pm J, \dots, \pm J, \uparrow (\downarrow)\rangle$ . Orange arrows along and between energy levels indicate population transfer between the states on a tracing field; the largest orange arrow is symbolic of a sequence of phonon-emission events required to relax the system back to the conducting parallel ground state orientation. (b) Loops of hysteresis in the calculated conductance on a trace (blue) and retrace (red) of a longitudinal magnetic field for the TbPc<sub>2</sub> molecular spin valve consisting of  $M$  TbPc<sub>2</sub> nanomagnets.

between the conducting ground state of the device and the  $M$  single-Tb-flipped levels, e.g.,  $|J, \dots, -J, \dots, J\rangle$ .

To further characterize our microscopic Coulomb blockade transport model, we now investigate the bias voltage dependence of the steady-state differential conductance for a range of applied, static magnetic field strengths. In Fig. 7, we report the steady-state conductance for the  $M = 2$  molecular spin valve at  $T = 30$  mK, in line with a recent CNT molecular spin valve experiment [26]. We note that at this resonance, the conductance has a pronounced peak about zero bias voltage, which broadens with the application of a magnetic field. The peak at zero bias in Fig. 7 can be understood with reference to the magnetic-field dependence of the energies reported in Fig. 2 wherein, at  $B_z = 0$ , the level degeneracy between the conducting neutral and reduced states is exact, only to be lifted gradually with the application of the magnetic field, resulting in a partial suppression of the conductance. We note that this behavior at the  $N/N + 1$  charge resonance point of our model is at odds with the experimental observation [26] of a drop of magnetoconductance or finite transport gap at zero bias voltage in the absence of a magnetic field, which is then resumed in the presence of a magnetic field.

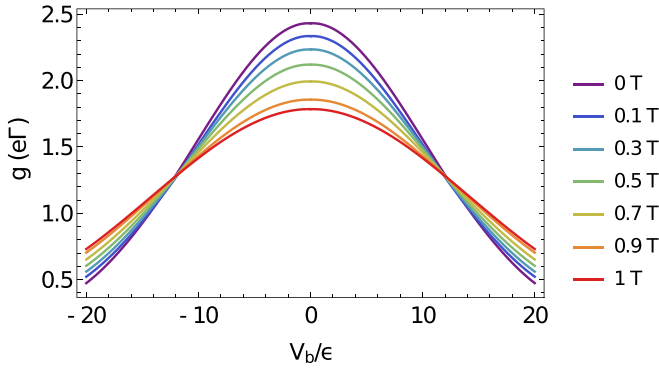


FIG. 7. Calculated steady-state conductance at  $T = 30$  mK as a function of bias voltage at the  $N/N + 1$  level degeneracy when the device is subject to various strengths of static, longitudinal magnetic field.

In an attempt at identifying other transport states of our model device displaying the experimentally observed dynamical spin valve effect but also reproducing the static transport gap observations [26], we turn our attention to the  $N + 1/N + 2$  charge resonance point, achieved with a gate voltage  $V_g$  that brings the  $|\pm J, \pm J, \uparrow (\downarrow), -\rangle$  reduced states in resonance with the doubly charged states. The  $N + 2$  doubly charged states are obtained by numerical diagonalization of Eq. (1) in the strongly interacting regime  $U \gg t_h$ . The resulting energies are plotted in Fig. 8 as function of the longitudinal magnetic field. In contrast to the  $N$  electron case in which the neutral manifold is completely degenerate at zero applied field, with a choice of  $U = 500$  meV consistent with first-principles estimations of the charging energy of the Pc ligands [26,38], we find that the nonmagnetic configurations of the terbium moments become the ground states of the doubly charged device (see Fig. 8). The  $N + 2$  spin-singlet states take the general form

$$|\Phi_{m_{J,1}, m_{J,2}}^{(i)}\rangle = |m_{J,1}, m_{J,2}\rangle \otimes [a^{(i)} |\uparrow\downarrow\rangle_1 |0\rangle_2 + b^{(i)} |\uparrow\rangle_1 |\downarrow\rangle_2 + c^{(i)} |\downarrow\rangle_1 |\uparrow\rangle_2 + d^{(i)} |0\rangle_1 |\uparrow\downarrow\rangle_2], \quad (9)$$

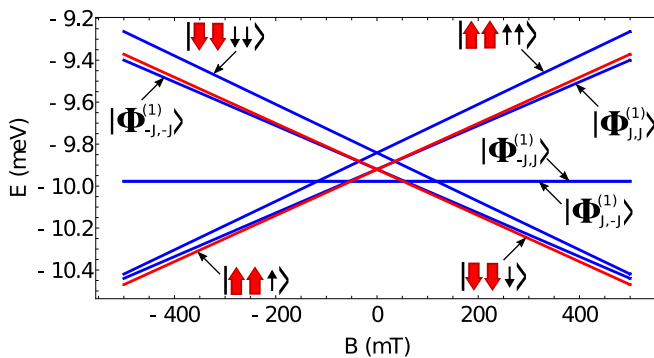


FIG. 8. Zeeman diagram of the most relevant lowest lying spin valve states for the reduced ( $N + 1$ , red) and doubly reduced ( $N + 2$ , blue) device obtained by the application of a gate detuning and diagonalization of Eq. (1) on the product basis of the nanomagnet angular momentum projections and dot spin states.

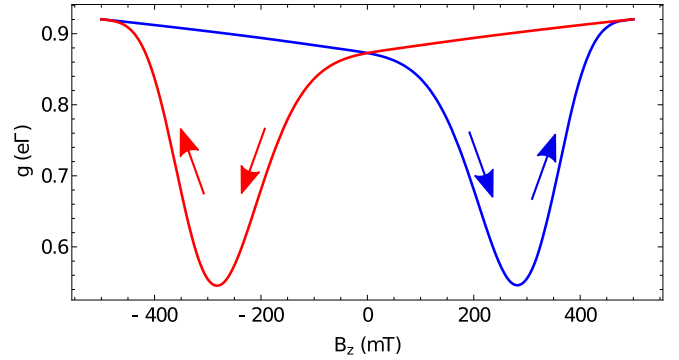


FIG. 9. Hysteresis of the magnetoconductance upon tracing (blue) and retracing (red) the longitudinal magnetic field, obtained at the  $N + 1/N + 2$  level degeneracy at  $T = 30$  mK and with a field sweep rate  $\omega = 0.005$  s $^{-1}$ .

wherein the amplitudes and energies of each state are reported in Appendix D. Strong on-site Coulomb repulsion and ferromagnetic coupling to the Tb magnets imply that the  $N + 2$  spin singlet states participating in low-temperature transport have the approximate form  $|\Phi_{J,-J}^{(1)}\rangle \approx |J, -J\rangle \otimes |\uparrow\rangle_1 |\downarrow\rangle_2$  and  $|\Phi_{-J,J}^{(1)}\rangle \approx |-J, J\rangle \otimes |\downarrow\rangle_1 |\uparrow\rangle_2$ , thus remaining nonconducting at low temperatures and bias voltages, since the singly reduced states  $|\pm J, \mp J, \uparrow (\downarrow), -\rangle$  are destabilized by the ferromagnetic coupling, hence thermally inaccessible for transport.

Next, we calculate the time-dependent magnetoconductance at  $T = 30$  mK in a sweeping longitudinal field traced and retraced across the device at a field sweep speed of  $\omega = 0.005$  s $^{-1}$ . The results are reported in Fig. 9, where it is evident that also at this new  $N + 1/N + 2$  charge resonance point, the differential conductance displays sharp jumps as a function of the time-dependent tracing and retracing sweeping field, giving rise to a hysteresis of the magnetoconductance that is akin to what we obtained at the resonance  $N/N + 1$  and is the hallmark of the dynamical spin-valve behavior of this supramolecular device.

The manifestation of hysteretic magnetoresistance at the  $N + 1/N + 2$  charge resonance can be understood in similar terms to that at the  $N/N + 1$  charge resonance. From Fig. 8, the ground state of the device at the beginning of a trace cycle (i.e., at negative magnetic field) is the fully polarized ferromagnetic reduced state which stays approximately in resonance with the doubly charged  $|\Phi_{J,J}^{(1)}\rangle$  state, thus leading to a nonzero conductance measurement at negative fields. After zero field is crossed, a two-step phonon emission cascade relaxes the device to the conducting  $|\Phi_{-J,-J}^{(1)}\rangle$  state but does so via the nonconducting  $|\Phi_{\pm J, \mp J}^{(1)}\rangle$  states, leading to the dip and subsequent revival of the magnetoconductance on the completion of the trace. A symmetrical mechanism is then observed upon dynamical reversal of the field direction during the retracing sweep.

Finally, we investigate the steady-state conductance at the  $N + 1/N + 2$  resonance, when a static magnetic field is applied to the device. In Fig. 10, we report the electrical conductance of the molecular spin valve device as a function of bias voltage at  $T = 30$  mK and zero magnetic field. Without a magnetic field, only the nonconducting ground states  $|\Phi_{\pm J, \mp J}^{(1)}\rangle$



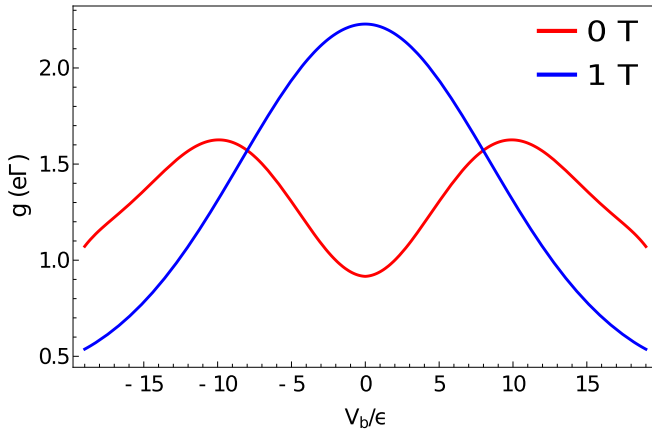


FIG. 10. Calculated steady-state conductance as a function of bias voltage with and without the application of a static magnetic field  $B_z = 0$  T (red) and  $B_z = 1$  T (blue).

of the spin valve are populated (see Fig. 8), leading to a conductance suppression at zero bias voltage. As bias voltage is increased, the conductance grows due to the population of the conducting all-parallel spin configurations of the spin valve. When a magnetic field of 1 T is applied to the device, the fully spin-polarized parallel configuration of the terbium magnetic moments becomes the ground state of the device. At this value of magnetic field, the level degeneracy between the fully spin-polarized  $N + 2$  doubly charged state and the  $N + 1$  singly charged all-parallel spin configuration of the terbium moments (as per Fig. 8) is preserved within the charge transport window allowed by level broadening and temperature, leading to an enhanced value of the conductance at zero bias with respect to the zero magnetic field case. Thus our model can capture the transport gap observed in experiments [26], albeit only at the  $N + 1/N + 2$  charge resonance point, crucially, within a fully incoherent transport regime where it is arguably not straightforward to account for a ballistic transport Fano-resonance conductance suppression effect [26,27].

#### IV. CONCLUSIONS

We have developed and used a time-dependent rate equation model within the adiabatic approximation to calculate the electrical conductance within the Coulomb blockade regime through a sequence of quantum dots coherently hybridized with  $\text{TbPc}_2$  molecular nanomagnets, and coherently coupled in a chain configuration, in the presence of an oscillating magnetic field. Our Coulomb blockade microscopic time-dependent model of the charge and spin dynamics of the spin-valve device, also accounting for dissipative spin-phonon relaxation mechanism of the nanomagnets grafted to the nanojunction, was shown here to be capable of capturing the experimentally observed hysteresis dynamics of the magnetoconductance, including its dependence on the sweep rate of the magnetic field  $\omega$  and on temperature.

To rationalize the occurrence of the hysteresis of the magnetoconductance and its behavior as a function of external parameters, we identified a microscopic mechanism based solely on phonon-assisted spin flips of the  $M$   $\text{TbPc}_2$  Ising magnetic moments, resulting in a sequential cascade

of population transfer between the two oppositely polarized conducting configurations (all spins parallel), mediated by the remaining  $2^M - 2$  nonconducting configurations of the supramolecular spin array. The proposed mechanism also allowed us to explicitly correlate the temperature dependence of the hysteretic spin-valve effect with the exchange coupling strength between  $\text{Tb(III)}$   $4f$  electrons and the sequential tunneling electron. We also investigated the conductance loops as a function of Tb chain length  $M$  and noted that as  $M$  increased, the deeper the conductance troughs became as a function of the tracing field, consistent with the proposed phonon-assisted multiple spin-reversal relaxation mechanism. Finally, we investigated the steady-state limit of our model, which could reproduce the presence of a finite transport gap in the magnetoconductance observed in experiments, without a reference to the coherent ballistic transport Fano-resonance argument utilized in previous studies.

In conclusion, we believe that our proposed microscopic model of time-dependent dissipative quantum transport offers a consistent and comprehensive picture of the physics involved in the experimentally observed supramolecular spin-valve effect, which explicitly accounts for the modulation of the transport dynamics of the device caused by the slow magnetic relaxation of SMMs grafted on its surface, which explains both the microscopic origin of the observed kinetic spin-valve effect (hysteresis of the magnetoconductance) and of the giant magnetoresistance effect observed in static magnetic fields, within a Coulomb blockade transport picture fully consistent with experimental observations. Our model also predicts a correlation between the observed drop of magnetoconductance in zero field, and the number of grafted molecular nanomagnets, which could be tested in future experiments.

These findings are expected to be useful for the design and interpretation of future experiments in molecular electronics advancing the quest for the ultimate miniaturization of spintronics devices using SMMs.

#### ACKNOWLEDGMENTS

K.H. acknowledges support from the Australian Government Research Training Program Scholarship. A.S. acknowledges support from the Australian Research Council (Future Fellowship No. FT180100519).

#### APPENDIX A: MODEL OF DISORDERED $\text{TbPc}_2$ QUANTIZATION AXES

In the main text, we have assumed for simplicity that the nanomagnets grafted to the  $sp^2$  hybridized surface share the same quantization axis, however, under experimental conditions this pristine configuration may be difficult to actualize. To investigate the effect of introducing noncollinear quantization axes for the  $\text{TbPc}_2$  nanomagnets, we return to the prototypical  $M = 2$  nanomagnet model and focus again on the  $N/N + 1$  charge resonance. We take the second in the series of nanomagnets to be quantized along the  $z'$  axis that is obtained from the quantization axis of the first nanomagnet by a rotation of  $\theta$  about the in-plane transverse axis of the device (see Fig. 11).

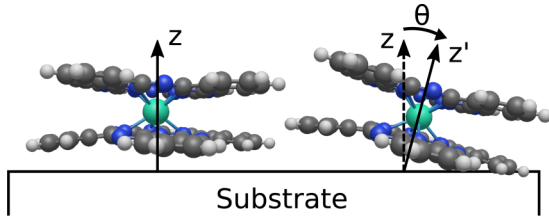


FIG. 11. Schematic depiction of the  $M = 2$  TbPc<sub>2</sub> molecular spin valve wherein the nanomagnets do not share the same quantization axes. Without loss of generality (WLOG) we take the first nanomagnet in the series to be quantized along the  $z$  axes and the second along the  $z'$  axes which is obtained by a rotation of the  $z$  axis by an angle  $\theta$  about the in-plane transverse axis of the device.

The Hamiltonian given in Eq. (1) is modified to account for the noncollinear magnetic anisotropy axes of the TbPc<sub>2</sub> nanomagnets, accordingly,

$$\begin{aligned}
 H_S(t) = & (\epsilon_1 - eV_g)c_{1\sigma}^\dagger c_{1\sigma} + (\epsilon_2 - eV_g)c_{2\sigma}^\dagger c_{2\sigma} \\
 & + \mu_B B_z(t) [g_J(J_z^1 + J_z^2 \cos \theta) + g(s_z^1 + s_z^2 \cos \theta)] \\
 & - a_1 J_z^1 s_z^1 - a_2 J_z^2 s_z^2 + t_h^* [\cos \theta (c_{1\uparrow}^\dagger c_{2\uparrow} + c_{1\downarrow}^\dagger c_{2\downarrow}) \\
 & - \sin \theta (c_{1\uparrow}^\dagger c_{2\downarrow} - c_{1\downarrow}^\dagger c_{2\uparrow})] + \text{H.c.}, \quad (\text{A1})
 \end{aligned}$$

where the primes indicate operators quantized along the  $z'$  axis. Owing to a stabilizing interaction between the bulky pyrene substituents (chemically grafted to the Pc ligands of the nanomagnets) and the  $sp^2$  hybridized surface, only small deviations of the TbPc<sub>2</sub> magnetic anisotropy axis from the substrate surface normal are expected [30]. Since  $\theta$  is small, the interligand hopping integrals  $t_h$  can to a good approximation be considered constant as a function of the canting angle. With this in mind, we proceed as in the main text and compute the magnetoconductance of the canted system noting that now, by virtue of the spin-flip hopping term proportional to  $t_h \sin \theta$  in Eq. (A1), the eigenstates of the reduced system are linear combinations of *both* radical spins delocalized across the Pc ligands of each nanomagnet,

$$\begin{aligned}
 |m_{J,1}, m_{J,2}, 1 \leq i \leq 4\rangle = & |m_{J,1}, m_{J,2}\rangle \otimes [e^{(i)} |\uparrow\rangle_1 |0\rangle_2 \\
 & + f^{(i)} |\downarrow\rangle_1 |0\rangle_2 + g^{(i)} |0\rangle_1 |\uparrow\rangle_2 \\
 & + h^{(i)} |0\rangle_1 |\downarrow\rangle_2], \quad (\text{A2})
 \end{aligned}$$

where the time-dependent coefficients  $e^{(i)}$ ,  $f^{(i)}$ ,  $g^{(i)}$ , and  $h^{(i)}$  are obtained from numerical diagonalization of each  $4 \times 4$   $m_{J,1}, m_{J,2}$  block of the Hamiltonian in Eq. (A1).

In Fig. 12, we plot  $\delta g = g_{\text{trace}} - g_{\text{retrace}}$  for a range of canting angles  $\theta$ . Notably, for larger values of the canting angle, the kinetic spin-valve effect is quenched. To understand why this is, recall that in the collinear quantization axes case that is explored in the main text, the conductance troughs characteristic of the kinetic spin-valve effect result from the transient population of the states with an antiparallel TbPc<sub>2</sub> magnetic moment configuration (see Fig. 2). Since the reduced states with antiparallel TbPc<sub>2</sub> magnetic moments are thermally inaccessible for transport (owing to the energetically unfavorable exchange interaction between the radical and one of the nanomagnets), the population of the neutral,

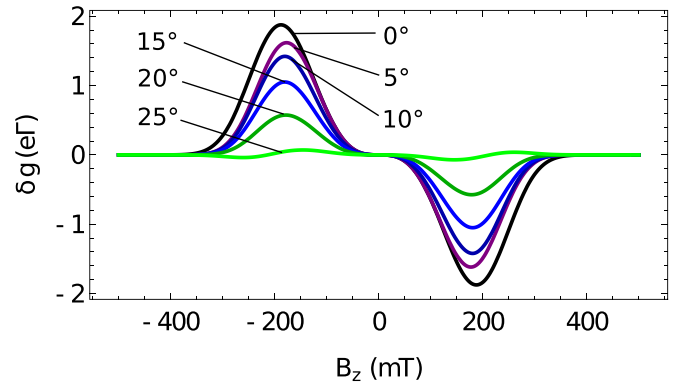


FIG. 12.  $\delta g$  calculated for various tilting angles  $\theta$  with a field sweeping rate  $\omega = 0.005 \text{ s}^{-1}$  and  $T = 0.1 \text{ K}$ . As  $\theta$  increases, the spin-valve effect is quenched as the reduced states for the antiparallel configuration of the TbPc<sub>2</sub> magnetic moments become stabilized and therefore begin to participate in transport.

nonconducting, antiparallel configuration of the TbPc<sub>2</sub> spin states leads to a drop in the conductance. In the tilted case, the presence of the spin-flip hopping term proportional to  $t_h \sin \theta$  in Eq. (A1) stabilizes the reduced states with antiparallel TbPc<sub>2</sub> orientations and thus the population of these nonmagnetic states no longer leads to a drop in the conductance.

## APPENDIX B: EXACT DIAGONALIZATION OF THE $M = 2$ CASE

When  $M = 2$  and doubly charged states of the device are neglected, the Hamilton in Eq (1) can be diagonalized exactly on the basis  $|m_{J,1}, m_{J,2}\rangle \otimes |\sigma\rangle$  ( $m_{J,i} = \pm J$ ). The adiabatic energies  $E_N$  for each charge state  $N$  are

$$\begin{aligned}
 E_0(m_{J,1}, m_{J,2}) &= g_J(m_{J,1} + m_{J,2})\mu_B B_z(t), \\
 E_1(m_{J,1}, m_{J,2}, \sigma, \pm) &= (\mathcal{E}^{(1)} + \mathcal{E}^{(2)})/2 \pm \Delta_{m_{J,1}, m_{J,2}, \sigma} \\
 &\quad + (g_J(m_{J,1} + m_{J,2}) + g\sigma)\mu_B B_z(t), \quad (\text{B1})
 \end{aligned}$$

where the splitting is given by  $\Delta_{m_{J,1}, m_{J,2}, \sigma} = \sqrt{\frac{1}{4}(\mathcal{E}^{(1)} - \mathcal{E}^{(2)})^2 + |t_h|^2}$  and  $\mathcal{E}^{(i)} = \epsilon_i - eV_g - a_i m_{J,i} \sigma$ . The eigenstates of  $H_S(t)$  in the neutral case are product states between the Ising-like spin states of the terbium nanomagnets and in the charged case are  $|m_{J,1}, m_{J,2}, \sigma, \pm\rangle = |m_{J,1}, m_{J,2}\rangle \otimes [u^\pm(m_{J,1}, m_{J,2}, \sigma) |\sigma\rangle_1 |0\rangle_2 + v^\pm(m_{J,1}, m_{J,2}, \sigma) |0\rangle_1 |\sigma\rangle_2]$ . The coefficients  $u^\pm$  and  $v^\pm$  for a given orientation of the Tb moments  $m_{J,1}$  and  $m_{J,2}$  and conduction electron spin  $\sigma$  are

$$\begin{aligned}
 u^\pm(m_{J,1}, m_{J,2}, \sigma) &= \frac{|t_h|}{\sqrt{2\Delta}} \frac{1}{\sqrt{\Delta \mp (\mathcal{E}^{(1)} - \mathcal{E}^{(2)})/2}}, \\
 v^\pm(m_{J,1}, m_{J,2}, \sigma) &= \mp \frac{\Delta \pm (\mathcal{E}^{(1)} - \mathcal{E}^{(2)})/2}{\sqrt{2\Delta}\sqrt{\Delta \mp (\mathcal{E}^{(1)} - \mathcal{E}^{(2)})/2}}, \quad (\text{B2})
 \end{aligned}$$

where  $\Delta = \Delta_{m_{J,1}, m_{J,2}, \sigma}$  has been introduced for notational convenience.

### APPENDIX C: NATURE OF THE DIRECT RELAXATION PROCESS IN TbPc<sub>2</sub>

The simplest effective crystal-field Hamiltonian that captures the energy splitting of the lowest  $J = 6$  spin-orbit multiplet of TbPc<sub>2</sub> is

$$H_{\text{cf}} = \alpha A_2^0 \langle r^2 \rangle O_2^0 + \beta [A_4^0 \langle r^4 \rangle O_4^0 + A_4^4 \langle r^4 \rangle O_4^4] + \gamma A_6^0 \langle r^6 \rangle O_6^0, \quad (\text{C1})$$

where  $\alpha$ ,  $\beta$  and  $\gamma$  are Stevens parameters,  $A_q^k \langle r^q \rangle$  are crystal-field parameters and  $O_q^k$  are Stevens operators [39]. In a previous experimental work [40], TbPc<sub>2</sub> nanomagnets deposited on a CNT in a nanoelectromechanical setup were shown to hybridize strongly to a longitudinal stretching mode in the CNT [denoted by the displacement function  $\delta u(\mathbf{r})$ ] that induced a rotation  $\delta \phi = \nabla \times \delta u(\mathbf{r})$  about the  $z$  axis of the TbPc<sub>2</sub> nanomagnets resulting in vibronic corrections to the crystal-field Hamiltonian given in Eq. (C1). Implementing this strong coupling into our model amounts to calculating the vibronically corrected Hamiltonian  $H' = \exp(i\delta \phi J_z / \hbar) H_{\text{cf}} \exp(-i\delta \phi J_z / \hbar)$  after which (to first order in  $\delta \phi$ ) we retrieve the equilibrium Hamiltonian  $H_{\text{cf}}$  and a spin-phonon coupling term proportional to  $g_{\text{s-ph}} O_4^4$ , where  $g_{\text{s-ph}}$  is a coupling constant specific to the underlying substrate.

The resultant spin-phonon coupling term causes transitions between the crystal-field states of the TbPc<sub>2</sub> nanomagnets that we treat within a Fermi golden rule approach and after standard manipulations [41] arrive at the formula

$$\Omega^{\pm J \rightarrow \mp J} = \pm \frac{2}{\sigma_m \hbar^2 c_s^4} |g_{\text{s-ph}}|^2 |\langle \mp J | O_4^4 | \pm J \rangle|^2 \times \frac{\omega_{\mp J, \pm J}^2}{1 - \exp(\omega_{\mp J, \pm J} / k_B T)}, \quad (\text{C2})$$

where  $\sigma_m = m/A$  is the mass per unit area of the substrate and  $c_s$  is the speed of sound in the substrate. Naturally, if  $|\pm J\rangle$  were a pure  $m_J = \pm J$  total angular momentum eigenstate, then the matrix element appearing in Eq. (C2) would be exactly zero. However, by virtue of the nonaxial harmonic  $\beta A_4^4 \langle r^4 \rangle O_4^4$  term appearing in the equilibrium crystal-field Hamiltonian from Eq. (C1), the TbPc<sub>2</sub> ground doublet contains some small component of the  $|m_J = \pm 2\rangle$  states, even for nonzero magnetic field, hence the matrix element in Eq. (C2) can be nonzero, i.e., the  $|m_J = \pm 2\rangle$  components of the ground doublet can be coupled by the spin-phonon Hamiltonian.

The matrix element in Eq. (C2) can be obtained by first calculating the correction to the  $|\pm J\rangle$  states at an applied mag-

netic field to first order in the crystal-field operator  $\beta A_4^4 \langle r^4 \rangle O_4^4$ . The corrections to each wave function are

$$\delta |J = \pm 6\rangle = \sum_{m \neq \pm 6} \frac{\langle m | \beta A_4^4 \langle r^4 \rangle O_4^4 | \pm 6 \rangle}{E_{\pm 6} - E_m} |m\rangle \approx \frac{\beta A_4^4 \langle r^4 \rangle}{2\Delta E} \prod_{m=\pm 6}^{\pm 2} \sqrt{J(J+1) - m(m \mp 1)} | \pm 2 \rangle, \quad (\text{C3})$$

where the energy gap between  $|\pm 6\rangle$  and  $|\pm 2\rangle$  in the denominator remains roughly unchanged from the case of zero applied field and so we have collected it into the constant term  $\Delta E \approx 60$  meV. By identifying the prefactor  $(2/\sigma_m \hbar^2 c_s^4) |g_{\text{s-ph}}|^2 |\langle \mp J | O_4^4 | \pm J \rangle|^2$  with  $\gamma_{\text{sp}}$ , we arrive at the effective expression for the phonon-mediated magnetic moment reversal rate in TbPc<sub>2</sub> reported in Eq. (6).

### APPENDIX D: ENERGIES AND AMPLITUDES OF $N + 2$ STATES DEFINED IN EQ. (9)

In this Appendix, Table I shows the numerical eigenvalues (energies) and the amplitudes of the  $N + 2$  quantum dot singlet states of the  $M = 2$  spin valve device defined in Eq. (9) which were obtained by diagonalizing the Hamiltonian with  $B_z = 0$  given in Eq. (1).

TABLE I. Composition of the  $N + 2$  singlet states. Numerical eigenvalues (energies) and amplitudes of the doubly reduced singlet states of the  $M = 2$  molecular spin valve presented in Eq. (9).

State	$E_2$ (meV)	$a^{(i)}$	$b^{(i)}$	$c^{(i)}$	$d^{(i)}$
$\Phi_{J,J}^{(1)}$	-9.92	0.01	-0.71	-0.71	0.01
$\Phi_{J,J}^{(2)}$	-9.72	0	0.71	-0.71	0
$\Phi_{J,J}^{(3)}$	490.28	0.71	0	0	-0.71
$\Phi_{J,J}^{(4)}$	490.48	0.71	0.01	0.01	0.71
$\Phi_{-J,J}^{(1)}$	-9.98	0.01	-0.34	-0.94	0.01
$\Phi_{-J,J}^{(2)}$	-9.66	0.01	-0.94	0.34	0.01
$\Phi_{-J,J}^{(3)}$	490.28	-0.71	0	0	0.71
$\Phi_{-J,J}^{(4)}$	490.48	0.71	0.01	0.01	0.71
$\Phi_{J,-J}^{(1)}$	-9.98	0.013	-0.94	-0.34	0.01
$\Phi_{J,-J}^{(2)}$	-9.66	0.01	0.34	-0.94	0.01
$\Phi_{J,-J}^{(3)}$	490.28	0.71	0	0	-0.71
$\Phi_{J,-J}^{(4)}$	490.48	0.71	0.01	0.01	0.71
$\Phi_{-J,-J}^{(1)}$	-9.92	0.01	-0.71	-0.71	0.01
$\Phi_{-J,-J}^{(2)}$	-9.72	0	0.71	-0.71	0
$\Phi_{-J,-J}^{(3)}$	490.28	0.71	0	0	-0.71
$\Phi_{-J,-J}^{(4)}$	490.48	0.71	0.01	0.01	0.71

- [1] G. Binasch, P. Grünberg, F. Saurenbach and W. Zinn, Enhanced magnetoresistance in layered magnetic structures with antiferromagnetic interlayer exchange, *Phys. Rev. B* **39**, 4828 (1989).  
 [2] M. N. Baibich, J. M. Broto, A. Fert, F. N. Van Dau, F. Petroff, P. Etienne, G. Creuzet, A. Friederich and J. Chazelas, Giant Magnetoresistance of (001) Fe/(001) Cr Magnetic Superlattices, *Phys. Rev. Lett.* **61**, 2472 (1988).

- [3] J. Barnaś and I. Weymann, Spin effects in single-electron tunneling, *J. Phys. Condens. Matter* **20**, 423202 (2008).  
 [4] R. Pati, L. Senapati, P. M. Ajayan and S. K. Nayak, First-principles calculations of spin-polarized electron transport in a molecular wire: Molecular spin valve, *Phys. Rev. B* **68**, 100407 (2003).

- [5] L. Zhu, K. L. Yao and Z. L. Liu, Molecular Spin Valve and Spin Filter Composed of Single-Molecule Magnets, *Appl. Phys. Lett.* **96**, 082115 (2010).
- [6] F. Zu, Z. Liu, K. Yao, G. Gao, H. Fu, S. Zhu, Y. Ni, and L. Peng, Nearly perfect spin filter, spin valve and negative differential resistance effects in a Fe 4-based single-molecule junction, *Sci. Rep.* **4**, 4838 (2014).
- [7] F.-X. Zu, G.-Y. Gao, H.-H. Fu, L. Xiong, S.-C. Zhu, L. Peng and K.-L. Yao, Efficient Spin Filter and Spin Valve in a Single-Molecule Magnet Fe<sub>4</sub> Between two Graphene Electrodes, *Appl. Phys. Lett.* **107**, 252403 (2015).
- [8] N. Ishikawa, M. Sugita, T. Ishikawa, S. Koshihara, and Y. Kaizu, Lanthanide double-decker complexes functioning as magnets at the single-molecular level, *J. Am. Chem. Soc.* **125**, 8694 (2003).
- [9] N. Ishikawa, M. Sugita, T. Okubo, N. Tanaka, T. Iino and Y. Kaizu, Determination of ligand-field parameters and f-electronic structures of double-decker bis (phthalocyaninato) lanthanide complexes, *Inorg. Chem.* **42**, 2440 (2003).
- [10] H. Wang, B.-W. Wang, Y. Bian, S. Gao and J. Jiang, Single-molecule magnetism of tetrapyrrole lanthanide compounds with sandwich multiple-decker structures, *Coord. Chem. Rev.* **306**, 195 (2016).
- [11] A. Candini, S. Klyatskaya, M. Ruben, W. Wernsdorfer, and M. Affronte, Graphene spintronic devices with molecular nanomagnets, *Nano Lett.* **11**, 2634 (2011).
- [12] M. Urdampilleta, N.-V. Nguyen, J.-P. Cleuziou, S. Klyatskaya, M. Ruben and W. Wernsdorfer, Molecular quantum spintronics: Supramolecular spin valves based on single-molecule magnets and carbon nanotubes, *Int. J. Mol.* **12**, 6656 (2011).
- [13] M. Urdampilleta, S. Klyatskaya, J.-P. Cleuziou, M. Ruben, and W. Wernsdorfer, Supramolecular spin valves, *Nat. Mater.* **10**, 502 (2011).
- [14] M. Urdampilleta, S. Klyatskaya, M. Ruben and W. Wernsdorfer, Magnetic interaction between a radical spin and a single-molecule magnet in a molecular spin-valve, *ACS Nano* **9**, 4458 (2015).
- [15] S. Thiele, F. Balestro, R. Ballou, S. Klyatskaya, M. Ruben, and W. Wernsdorfer, Electrically driven nuclear spin resonance in single-molecule magnets, *Science* **344**, 1135 (2014).
- [16] C. Godfrin, S. Lumetti, H. Biard, E. Bonet, S. Klyatskaya, M. Ruben, A. Candini, M. Affronte, W. Wernsdorfer and F. Balestro, Microwave-assisted reversal of a single electron spin, *J. Appl. Phys.* **125**, 142801 (2019).
- [17] R. Vincent, S. Klyatskaya, M. Ruben, W. Wernsdorfer, and F. Balestro, Electronic read-out of a single nuclear spin using a molecular spin transistor, *Nature* **488**, 357 (2012).
- [18] D. Komijani, A. Ghirri, C. Bonizzoni, S. Klyatskaya, E. Moreno-Pineda, M. Ruben, A. Soncini, M. Affronte and S. Hill, Radical-lanthanide ferromagnetic interaction in a Tb<sup>III</sup> bis-phthalocyaninato complex, *Phys. Rev. Mater.* **2**, 024405 (2018).
- [19] R. Pederson, A. L. Wysocki, N. Mayhall and K. Park, Multireference Ab initio studies of magnetic properties of terbium-based single-molecule magnets, *J. Phys. Chem. A* **123**, 6996 (2019).
- [20] H. Huang, W. Van den Heuvel and A. Soncini, Lanthanide-radical magnetic coupling in [LnPc<sub>2</sub>]<sup>0</sup>: Competing exchange mechanisms captured via ab initio multi-reference calculations, *Quantum Mater. Res.* **1**, e200003 (2020).
- [21] A. LodiRizzini, C. Krull, T. Balashov, J. J. Kavich, A. Mugarza, P. S. Miedema, P. K. Thakur *et al.*, Coupling Single Molecule Magnets to Ferromagnetic Substrates, *Phys. Rev. Lett.* **107**, 177205 (2011).
- [22] A. Candini, D. Klar, S. Marocchi, V. Corradini, R. Biagi, V. De Renzi, U. del Pennino, F. Troiani, V. Bellini, S. Klyatskaya, *et al.*, Spin-communication channels between Ln (III) bis-phthalocyanines molecular nanomagnets and a magnetic substrate, *Sci. Rep.* **6**, 1 (2016).
- [23] S. Marocchi, A. Candini, D. Klar, W. Van den Heuvel, H. Huang, F. Troiani, V. Corradini, R. Biagi, V. De Renzi, S. Klyatskaya, *et al.*, Relay-like exchange mechanism through a spin radical between TbPc<sub>2</sub> molecules and graphene/Ni(111) substrates, *ACS Nano* **10**, 9353 (2016).
- [24] T. Komeda, K. Katoh and M. Yamashita, Double-decker phthalocyanine complex: Scanning tunneling microscopy study of film formation and spin properties, *Prog. Surf. Sci.* **89**, 127 (2014).
- [25] C. Godfrin, A. Ferhat, R. Ballou, S. Klyatskaya, M. Ruben, W. Wernsdorfer and F. Balestro, Operating Quantum States in Single Magnetic Molecules: Implementation of Grover's Quantum Algorithm, *Phys. Rev. Lett.* **119**, 187702 (2017).
- [26] I. V. Krainov, J. Klier, A. P. Dmitriev, S. Klyatskaya, M. Ruben, W. Wernsdorfer and I. V. Gornyi, Giant magnetoresistance in carbon nanotubes with single-molecule magnets TbPc<sub>2</sub>, *ACS Nano* **11**, 6868 (2017).
- [27] K. Hong and W. Y. Kim, Fano-resonance-driven spin-valve effect using single-molecule magnets, *Angew.* **52**, 3389 (2013).
- [28] A. Płomińska and I. Weymann, Tunnel magnetoresistance of a supramolecular spin valve, *Europhys. Lett.* **125**, 18004 (2019).
- [29] N. Ishikawa, M. Sugita and W. Wernsdorfer, Quantum tunneling of magnetization in lanthanide single-molecule magnets: bis (phthalocyaninato) terbium and bis (phthalocyaninato) dysprosium anions, *Angewandte* **44**, 2931 (2005).
- [30] M. Lopes, A. Candini, M. Urdampilleta, A. Reserbat-Plantey, V. Bellini, S. Klyatskaya, L. Marty, M. Ruben, M. Affronte, W. Wernsdorfer and N. Bendiab, Surface-enhanced Raman signal for terbium single-molecule magnets grafted on graphene, *ACS Nano* **4**, 7531 (2010).
- [31] V. Dohm and P. Fulde, Magnetoelastic interaction in rare earth systems, *Z. Phys. B Condens. Matter* **21**, 369 (1975).
- [32] A. Lunghi, F. Totti, R. Sessoli and S. Sanvito, The role of anharmonic phonons in under-barrier spin relaxation of single molecule magnets, *Nat. Commun.* **8**, 14620 (2017).
- [33] H.-A. Engel and D. Loss, Single-spin dynamics and decoherence in a quantum dot via charge transport, *Phys. Rev. B* **65**, 195321 (2002).
- [34] K. R. Vignesh, A. Soncini, S. K. Langley, W. Wernsdorfer, K. S. Murray, and G. Rajaraman, *Nat. Commun.* **8**, 1 (2017).
- [35] K. Hyman and A. Soncini, Mechanisms of spin-charge conversion for the electrical readout of 4 f quantum states in a TbPc<sub>2</sub> single-molecule magnet spin transistor, *Phys. Rev. B* **102**, 045313 (2020).
- [36] C. Timm and F. Elste, Spin amplification, reading, and writing in transport through anisotropic magnetic molecules, *Phys. Rev. B* **73**, 235304 (2006).
- [37] M. Misiorny, and J. Barnaś, Spin polarized transport through a single-molecule magnet: Current-induced magnetic switching, *Phys. Rev. B* **76**, 054448 (2007).



- [38] L. Vitali, S. Fabris, A. M. Conte, S. Brink, M. Ruben, S. Baroni and K. Kern, Electronic structure of surface-supported bis (phthalocyaninato) terbium (III) single molecular magnets, [Nano Lett.](#) **8**, 3364 (2008).
- [39] A. Abragam and B. Bleaney, *Electron Paramagnetic Resonance of Transition Ions* (Oxford University Press, Oxford, 2012).
- [40] M. Ganzhorn, S. Klyatskaya, M. Ruben and W. Wernsdorfer, Strong spin–phonon coupling between a single-molecule magnet and a carbon nanotube nanoelectromechanical system, [Nat. Nanotechnol.](#) **8**, 165 (2013).
- [41] D. Gatteschi, R. Sessoli, and J. Villain, *Molecular Nanomagnets* (Oxford University Press on Demand, 2006).